JACS
JOURNAL OF THE AMERICAN CHEMICAL SOCIETY

pubs.acs.org/JACS Article

Synthetic Control of Intrinsic Defect Formation in Metal Oxide Nanocrystals Using Dissociated Spectator Metal Salts

Kihoon Kim, Jiwon Yu, Jungchul Noh, Lauren C. Reimnitz, Matthew Chang, Daniel R. Gamelin, Brian A. Korgel, Gyeong S. Hwang, and Delia J. Milliron*

Cite This: *J. Am. Chem. Soc.* 2022, 144, 22941−22949 Read Online

ACCESS | Metrics & More | Article Recommendations | Supporting Information

ABSTRACT: Crystallographic defects are essential to the functional properties of semiconductors, controlling everything from conductivity to optical properties and catalytic activity. In nanocrystals, too, defect engineering with extrinsic dopants has been fruitful. Although intrinsic defects like vacancies can be equally useful, synthetic strategies for controlling their generation are comparatively underdeveloped. Here, we show that intrinsic defect concentration can be tuned during the synthesis of colloidal metal oxide nanocrystals by the addition of metal salts. Although not incorporated in the nanocrystals, the metal salts dissociate at high temperatures, promoting the dissociation of carboxylate ligands from metal precursors, leading to the introduction of oxygen vacancies. For example, the concentration of oxygen vacancies can be controlled up to 9% in indium oxide nanocrystals. This method is broadly applicable as we demonstrate by generating intrinsic defects in metal oxide nanocrystals of various morphologies and compositions.

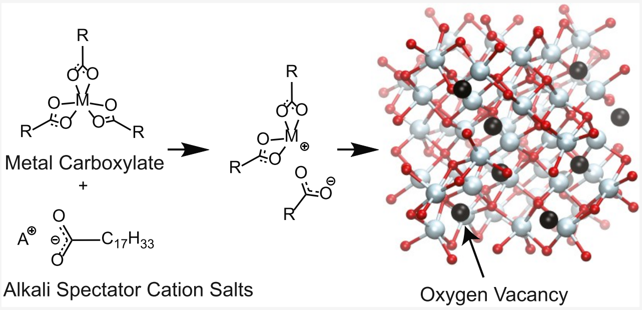

■ INTRODUCTION

Point defects control the properties of semiconductors from conductivity to light absorption and emission. In colloidal nanocrystals, the incorporation of extrinsic dopant defects (atomic impurities) has enabled the realization of spectrally tunable plasmon resonances, long-lived photoluminescence (PL), and quantum cutting and upconversion.[1−4] Synthetic control over the introduction of intrinsic defects (i.e., vacancies and interstitials) remains limited but holds great potential for defect engineering of distinct functionalities.[5] For example, oxygen vacancies (V_O), a common type of intrinsic defect in metal oxides, can generate deep trap states that influence light absorption and luminescence or boost the sensitivity of surface-enhanced Raman scattering.[6−10] V_O can also act as molecular adsorption sites, facilitating water splitting or other catalytic reactions.[11,12] They influence ionic conductivity and electronic properties, including the work function and electron concentration.[12−16]

Synthetic introduction of extrinsic defects during the growth of semiconductor nanocrystals has been demonstrated for various dopants and a wide range of host materials.[1,17−19] By tuning the kinetics of dopant incorporation, control over their spatial distribution within the nanocrystals has been accomplished.[20−22] These synthetic methods and the unraveling of their mechanisms have enabled the systematic study and optimization of wide-ranging dopant-derived properties in semiconductor nanocrystals.

In contrast to the development of extrinsic defect engineering, the synthetic control of intrinsic defects in nanocrystals is still limited.[23,24] From the study of bulk metal oxides, the concentration of oxygen vacancies, $[V_O]$, is known to depend on oxygen partial pressure.[25,26] Under low oxygen partial pressure, the equilibrium is shifted favoring the formation of V_O, but nanocrystals are grown under kinetic control and varying oxygen partial pressure during synthesis has not resulted in the precise tuning of defect-derived properties. More often, the lack of deliberate synthetic control has led researchers to regard $[V_O]$ as an uncontrollable parameter or, as for cadmium oxide (CdO) nanocrystals, one inextricably linked to nanocrystal size.[24] For this reason, postsynthetic tuning methods such as treating with hydrogen gas, ultraviolet irradiation in the presence of sacrificial molecules, or ion bombardment have been used.[7,8,27−29] However, besides the requirement of additional processing, these methods only affect the near-surface $[V_O]$, limiting which properties can be tuned and to what extent.

Received: August 16, 2022
Published: December 6, 2022

Here, we report a new approach to control intrinsic defect generation during the synthesis of colloidal metal oxide nanocrystals. We show that intrinsic defects can be generated by the addition of spectator metal salts that can be dissociated at the reaction temperature. Specifically, the addition of sodium oleate (NaOL) to the oleyl alcohol reaction medium, followed by the injection of indium carboxylate ($In(RCOO)_3$) precursor, results in a high $[V_O]$ in indium oxide (In_2O_3) nanocrystals, turning their color black. We simulated the coordination environment of the precursor by classical molecular dynamics (MD) and found that the added salt enhances the dissociation of $RCOO^-$ from In^{3+}. Considering the metal oxide formation mechanism, we propose that the resulting $RCOO^-$ deficiency in the precursor is responsible for V_O generation during crystal growth. By changing the initial amount of NaOL in the oleyl alcohol, the $[V_O]$ can be controlled up to 9% in In_2O_3 nanocrystals. We generalize the results by using potassium oleate (KOL) instead, generating black In_2O_3 nanocubes, and by synthesizing other defect-engineered metal oxide nanocrystal compositions, including iron oxide (γ-Fe_2O_3) and CdO.

■ RESULTS AND DISCUSSION

Synthesis of Black In_2O_3 Nanocrystals. The continuous injection method was used because it produces various metal oxide nanocrystals with control over size, shape, and incorporation of extrinsic defects.[20,21,30−32] We focused on In_2O_3 nanocrystals because of their intrinsic defect-driven properties such as PL and catalytic activity.[8,9,13,33−35] In_2O_3 nanocrystals synthesized by the injection of 7 mmol of $In(RCOO)_3$ precursor solution into oleyl alcohol resulted in pale yellow-colored nanocrystals with 23 nm diameter and a spherical morphology (Figure 1a). In contrast, the addition of NaOL to oleyl alcohol in advance of the injection of the $In(RCOO)_3$ precursor resulted in persistent black color from the beginning of precursor injection through isolation of the nanocrystals. The yield was reduced from 83 to 68%. Imaged by scanning electron microscopy (SEM), the 31 nm nanocrystals had a rhombic dodecahedral shape (Figure 1b). We previously observed the same morphology when NaOL was present in the injected precursor solution. However, its color was light gray and only when including NaOL in the reaction flask was the black color observed (further discussion below).[30]

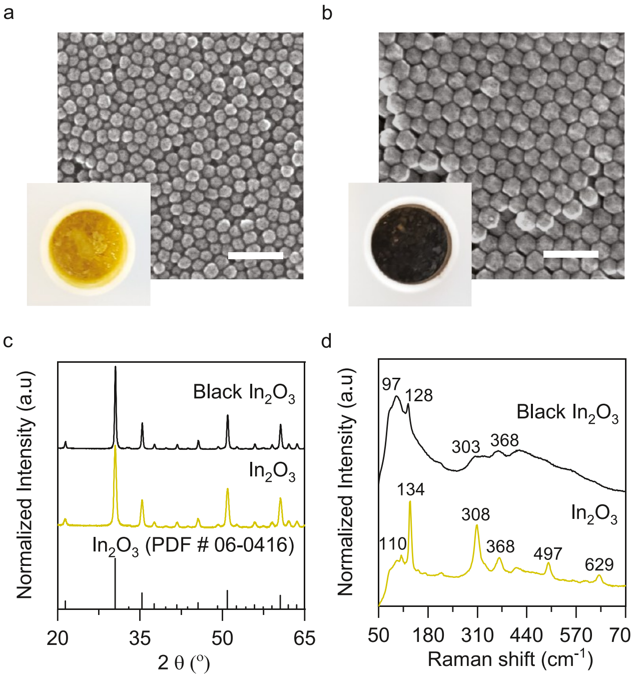

Figure 1. Synthesis of black In_2O_3 nanocrystals. SEM and photographs of (a) In_2O_3 nanocrystals synthesized without the addition of NaOL and (b) black In_2O_3 nanocrystals synthesized with NaOL in the reaction flask and precursor solution. Scale bars are 100 nm. (c) XRD patterns and (d) Raman spectra of nanocrystal powders.

Despite the color difference, the X-ray diffraction (XRD) patterns of both yellow and black nanocrystals exactly match the native In_2O_3 bixbyite cubic crystal structure (Figure 1c). However, while the yellow In_2O_3 nanocrystals show the sharp signature Raman peaks of the In_2O_3 bixbyite structure, Raman peaks of the black In_2O_3 nanocrystals were broadened with a notable shift to lower frequency (Figure 1d). These changes in the Raman spectrum can be explained by phonon confinement effects due to either finite size of the nanocrystals or shortening of the correlation length by the presence of lattice defects.[36−39] Considering that the black In_2O_3 nanocrystals are actually larger and that phonon confinement effects typically become significant only when nanocrystals are smaller than 20 lattice parameters, these Raman changes are attributed to lattice defects in the black In_2O_3 nanocrystals.[38] However, since no Na incorporation could be detected by energy-dispersive X-ray spectroscopy (EDS), X-ray photoelectron spectroscopy (XPS), or inductively coupled plasma mass spectrometry (ICP-MS), we conclude that intrinsic defects are responsible (Figures S1−S3). Indeed, the intrinsic defects changed the stoichiometric ratio between indium and oxygen, which is 1:1.37 in the black In_2O_3 nanocrystals but close to stoichiometric (1:1.5) in regular In_2O_3 nanocrystals after removing the ligands (Figure S1). This excess indium suggests the generation of intrinsic donor defects, either indium interstitials or V_O. Thermogravimetric analysis (TGA) in air shows a weight increase of around 600 °C for black In_2O_3 suggesting oxygen uptake, while a continuous weight loss was observed in In_2O_3 nanocrystals in this temperature range (Figure S4). After this annealing, the black color was lost, becoming yellow, and the Raman peaks both sharpened and shifted to higher frequency, all indicating defect curing. Besides, the lattice oxygen contribution to the O 1s peak in XPS is diminished for the black In_2O_3 nanocrystals, while there is no change in the indium 3d peak (Figure S2 and Table S1).[8] In small nanocrystals, nonstoichiometry is often related to the composition of the surface. However, since our nanocrystal size is relatively large, a volume effect is likely to be mainly responsible for the nonstoichiometry, as discussed further below.

Optical Characterization. As suggested by the black color, the intrinsic defects strongly impact the optical properties of the synthesized In_2O_3 nanocrystals. Analyzing the absorption spectra, the optical band gap of In_2O_3 nanocrystals is 3.7 eV, while black In_2O_3 nanocrystals have a lower band gap of 3.5 eV and an additional absorption tail stretching across the visible wavelength region (Figure 2a), which could be due to trap states within the band gap. Further indicators of trap state formation were found in the PL response. In In_2O_3 nanocrystals, a consistent, asymmetric PL peak at 2.7 eV was observed while the excitation energy varied from 5 to 3.5 eV (Figure 2b). Considering the 3.7 eV optical band gap, this PL peak could be from intrinsic trap states since it was observed even for sub-band-gap 3.5 eV excitation. Black

https://doi.org/10.1021/jacs.2c08716
J. Am. Chem. Soc. 2022, 144, 22941−22949

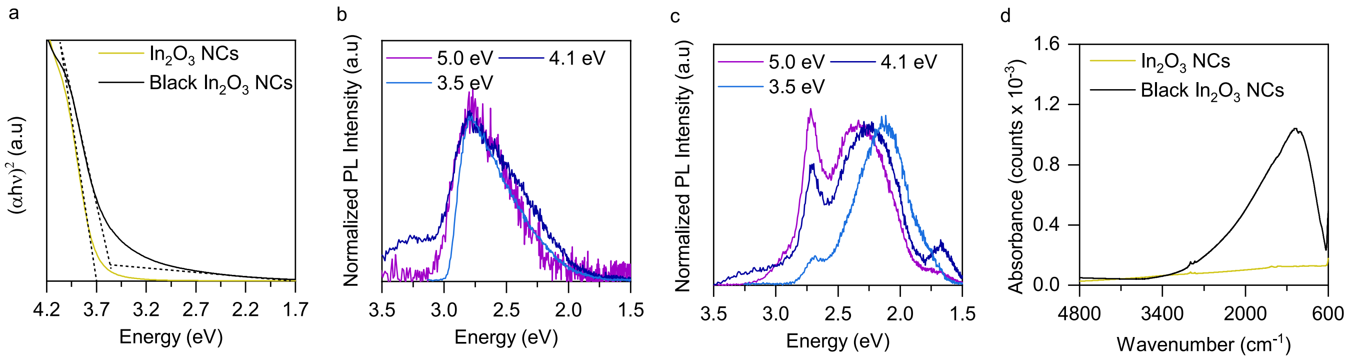

Figure 2. Optical response comparison of In_2O_3 and black In_2O_3 nanocrystals. (a) Tauc plot based on UV−vis absorption spectra measured in films. Dotted straight lines show the estimation of the optical band gaps. (b) PL spectra of In_2O_3 nanocrystals in hexane with different excitation energies. (c) PL spectra of black In_2O_3 nanocrystals in hexane with different excitation energies. (d) FTIR absorption spectra normalized by the thickness of nanocrystal films.

Scheme 1. Mechanism of V_O Generation Due to the Dissociation of $RCOO^-$ Enhanced by Dissociated NaOL[a]

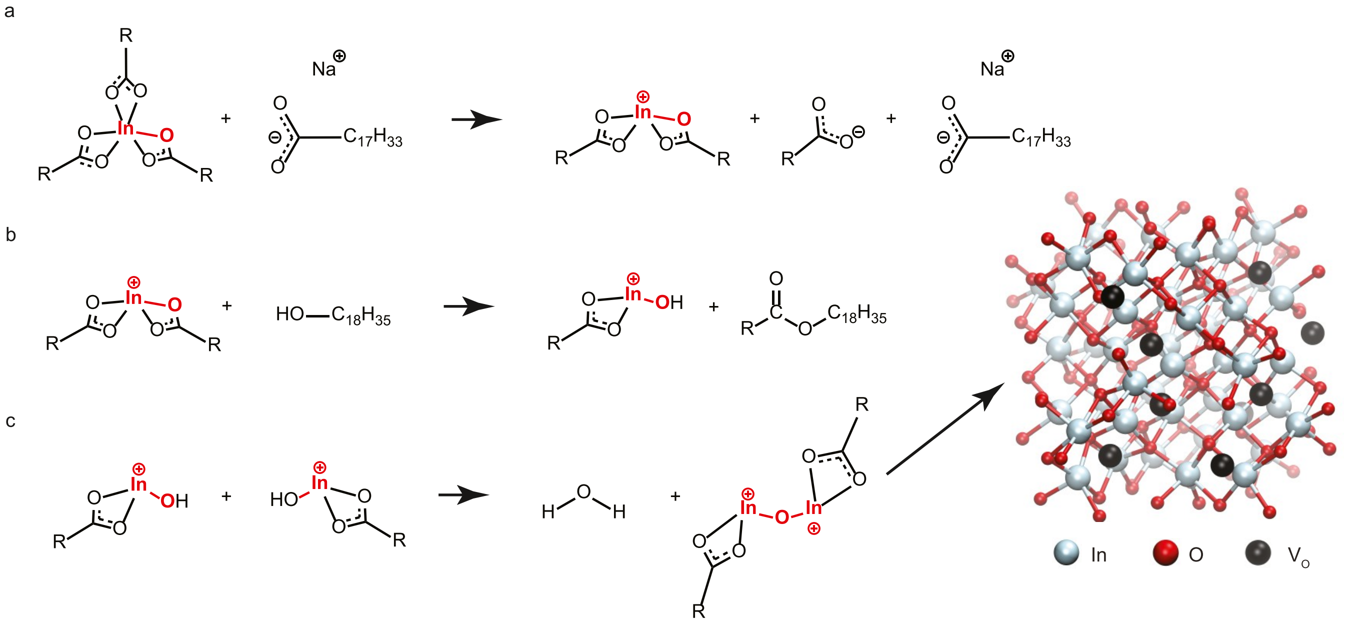

[a](a) Dissociation of $RCOO^-$ from $In(RCOO)_3$ due to the presence of the dissociated NaOL. (b) Esterification reaction between the $RCOO^-$-deficient $In(RCOO)_3$ and oleyl alcohol. (c) Condensation of indium hydroxide to form In_2O_3 lattice. $RCOO^-$-deficient moieties become V_O sites in the In_2O_3 lattice. Highlighted red moieties incorporate in the In_2O_3 lattice.

In_2O_3 nanocrystals also exhibited a primary PL peak at 2.7 eV when excitation energy varied from 5 to 3.5 eV (Figure 2c). However, there was an additional broad PL peak whose maximum shifted from 2.3 to 2.1 eV for longer excitation wavelength while also gaining intensity relative to the primary peak at 2.7 eV. In previous experimental and theoretical studies of In_2O_3, V_O were reported to be responsible for a broad PL peak at 2.3 eV, but there is no report about the excitation wavelength dependence of the PL.[34,40] We also observed strong free-electron absorption around 1000 cm^{-1} in a film of black In_2O_3 nanocrystals (Figure 2d), consistent with the presence of donor defects. Further evidence is found in the electron paramagnetic resonance (EPR) spectra. The signal for black In_2O_3 nanocrystals is much stronger than that for regular In_2O_3 nanocrystals, with a *g*-factor of 2.09 indicative of singly charged V_O (Figure S5).[34] Considering all of these observations and that the formation energy of V_O is lower than that of an indium interstitial at low oxygen partial pressure, we conclude that V_O are the main defect type in the black In_2O_3 nanocrystals, with free electrons and electrons localized on V_O sites providing charge balance.[40,41]

V_O Formation Mechanism. The lattice oxygen in In_2O_3 nanocrystals is understood to originate from bound $RCOO^-$ in the precursor complex, so we hypothesized that V_O formation is caused by *in situ* dissociation of the $In(RCOO)_3$ (Scheme 1a). During nanocrystal growth, oleyl alcohol acts as a nucleophile and reacts with $In(RCOO)_3$ to form an ester byproduct, liberating oxygen from the $RCOO^-$ to form the oxide crystal lattice (Scheme 1b,c).[30,32] Therefore, we studied the oxygen coordination number (CN) in the $In(RCOO)_3$ precursor using classical MD. For the simulation, we modeled the reaction environment precisely including the stoichiometry of the reagents, temperatures, and molecular structures (Figure S6). We assumed that $In(RCOO)_3$ contains two OL and one acetate (ac) and that NaOL is dissociating forming Na^+ and OL^- at this temperature, based on previous reports.[30,42−44]

Our results show that the total CN of oxygen to In^{3+} (CN_{Total}) without NaOL is 6.10, which is close to ideal stoichiometry (Table 1). However, the presence of dissociated NaOL reduced CN_{Total} to 4.28, which implies that ~30% of the $RCOO^-$ is dissociated from In^{3+}. We found that increasing [NaOL] results in a continuous decrease of CN_{Total} (Figure S7) in the $In(RCOO)_3$. In effect, Na^+ competes with In^{3+} for ionic bonding with $RCOO^-$, favoring additional dissociation in the higher ionic strength synthetic environment. The presence of Na^+ thus effectively lowers the chemical potential of $RCOO^-$ in the solution, shifting the equilibrium toward dissociation from the $In(RCOO)_3$. According to our calculations, the dissociation of both OL and ac is more favorable in the presence of dissociated NaOL but ac is more likely to be dissociated compared to OL. Experimentally, compared to In_2O_3 nanocrystals, a 67% reduction of surface $RCOO^-$ ligand density was observed in black In_2O_3 by TGA (Figure S4), which supports the dissociation of $RCOO^-$ in the presence of NaOL. More direct experimental evidence of the precursor speciation might be pursued in the future by in situ X-ray scattering or X-ray absorption spectroscopy. Besides, considering that the color of the solution is black throughout the precursor injection, during which the continuous growth of black In_2O_3 nanocrystals was confirmed by taking aliquots, we believe that V_O are located throughout the whole volume of the In_2O_3 nanocrystals (Figure S8).

Table 1. Comparison of Oxygen CN in $In(RCOO)_3$ Based on Classical MD Simulation[a]

additives	CN_{Total}	CN_{OL}	CN_{ac}
no NaOL	6.10 (±0.02)	4.22 (±0.09)	1.18 (±0.05)
with NaOL	4.28 (±0.07)	3.62 (±0.04)	0.66 (±0.07)
with NaOL/no NaOL	0.70	0.86	0.35

[a] CN_{OL} represents CN by OL and CN_{ac} indicates CN by ac.

Therefore, we propose that V_O are generated by the dissociation of $RCOO^-$, resulting in a $RCOO^-$ deficiency in the $In(RCOO)_3$ that becomes kinetically trapped as a lattice oxygen deficiency during nanocrystal growth (Scheme 1). This mechanism is similar to the kinetic incorporation mechanism for extrinsic dopants.[19,45] Just as long retention of extrinsic dopants at the surface of nanocrystals during growth increases dopant incorporation efficiency, we expect that matching the kinetics between the lifetime of the oxygen-deficient moieties and the growth of the In_2O_3 nanocrystal lattice is essential to

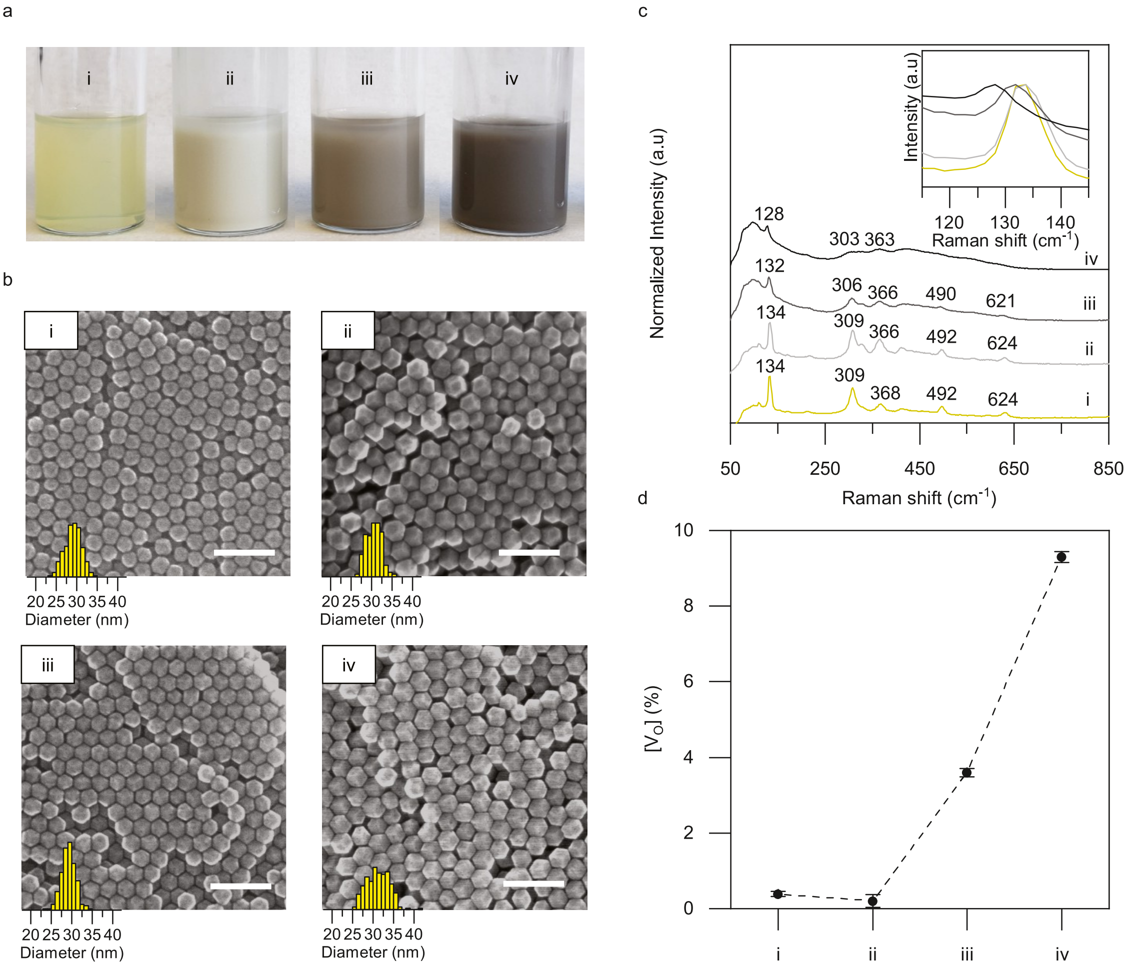

Figure 3. [V_O] control in In_2O_3 nanocrystals. (a) Picture of the In_2O_3 nanocrystal dispersions synthesized (i) without NaOL addition, (ii) with 19.5 mmol of NaOL in the precursor solution, (iii) with 6.5 mmol of NaOL in oleyl alcohol and 13.0 mmol in the precursor solution, and (iv) with 13.0 mmol of NaOL in oleyl alcohol and 6.5 mmol in the precursor solution. (b) SEM images of resulting nanocrystals and their size distributions. Scale bars are 100 nm. (c) Raman spectra (inset magnified). (d) Estimated [V_O] of In_2O_3 nanocrystal based on the Rietveld refinement of XRD patterns. Error bars indicate standard deviation.

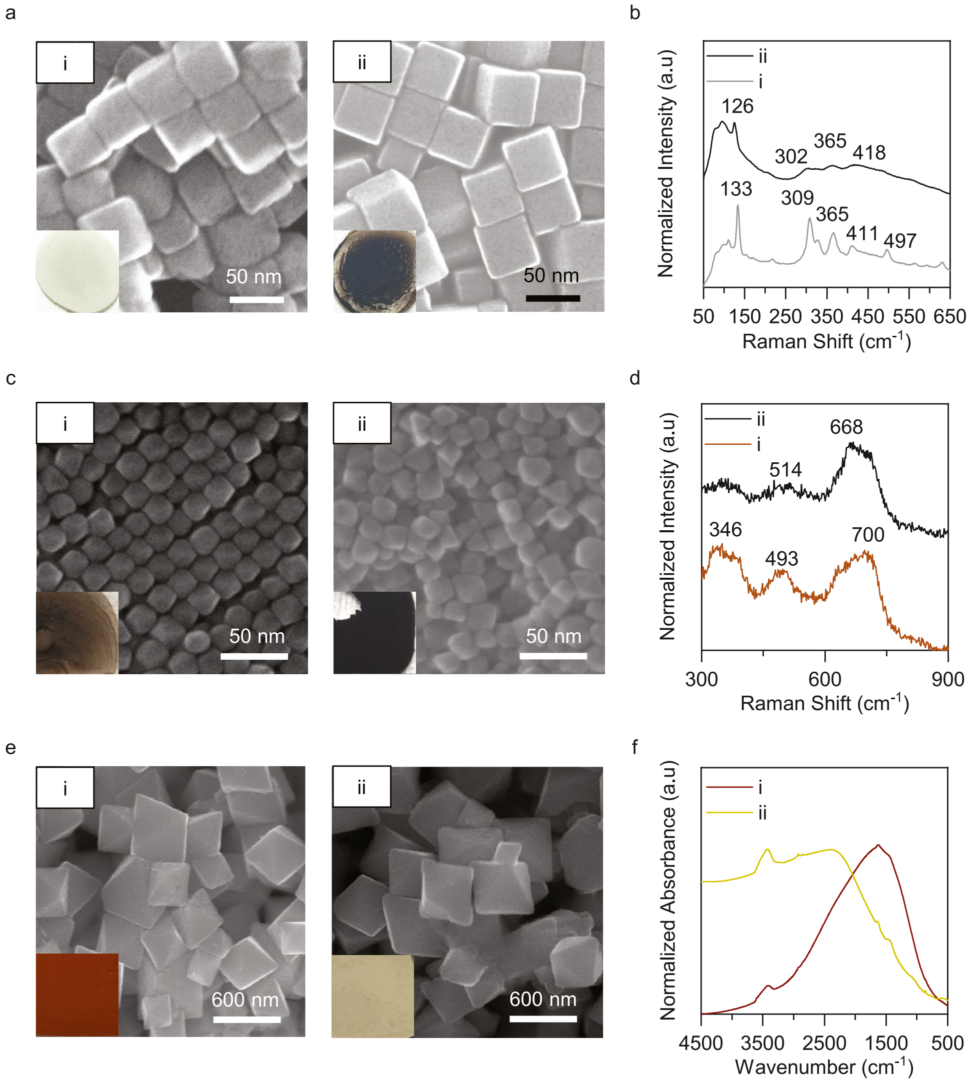

Figure 4. Demonstration of intrinsic defect generation in different systems. (a) SEM and powder images of In_2O_3 nanocubes synthesized (i) with 19.5 mmol of KOL in $In(RCOO)_3$ precursor solution and (ii) with 13.0 mmol of KOL in oleyl alcohol and 6.5 mmol in the precursor solution. (b) Raman spectra of In_2O_3 nanocrystals. (c) SEM and powder images of γ-Fe_2O_3 nanocrystals synthesized (i) without the addition of NaOL and (ii) with 13.0 mmol of NaOL in oleyl alcohol. (d) Raman spectra of γ-Fe_2O_3 nanocrystals. (e) SEM and powder images of CdO synthesized (i) without the addition of NaOL and (ii) with 0.8 mmol of NaOL in oleyl alcohol. (f) FTIR spectra of CdO films.

form V_O. Previously, carboxylate salts of group 13 metals were reported to catalyze copper oxide nanocrystal growth by reacting with oleyl alcohol.[46] However, in our case, there was no reaction between NaOL and oleyl alcohol even for high concentration at the reaction temperature.[30] Instead, the singly charged alkali metal cation favors dissociation due to the weak ionic bonding with their counteranions, facilitating the introduction of V_O in the growing In_2O_3 nanocrystals.

Control of [V_O]. As suggested by the MD simulation results, we found that the [NaOL] during the reaction could control the [V_O] in the resulting In_2O_3 nanocrystals. For reliable analysis, we tried to maintain a consistent size of nanocrystals to minimize confounding the influence on Raman spectra and XRD. Because NaOL addition increased nanocrystal size, the total amount of NaOL added to the reactor was fixed at 19.5 mmol while also maintaining the ratio between indium and total OL as 1:6.33. However, the distribution of NaOL between the oleyl alcohol synthetic medium and the $In(RCOO)_3$ precursor solution was varied to investigate the resulting change in [V_O] (Figure 3). Because temperature higher than 200 °C is required to dissociate the NaOL, we hypothesized that $In(RCOO)_3$ will not be dissociated before the injection to the hot oleyl alcohol synthetic medium even though it is already mixed with NaOL.[43,44] Regardless of the distribution of the NaOL, these In_2O_3 nanocrystals were consistently around 31 nm with a rhombic dodecahedral shape (Figure 3b). However, the color gradually changed from light gray to black for increasing the amount of NaOL in oleyl alcohol (Figure 3a). Even though the color was different, the Raman spectrum of In_2O_3 nanocrystals synthesized with the addition of NaOL only in the precursor solution was almost identical to that of nanocrystals synthesized without any NaOL (Figure 3c), although the increased intensity of Raman peaks related to V_O at 329, 366, and 409 cm^{-1} suggests at least a small increase in [V_O] (Figure 3c(ii)).[47] As more of the NaOL is added to the oleyl alcohol, the Raman peaks shift progressively to lower frequency and broaden, with increasing intensity of a broad background at 97 cm^{-1}. Especially the mode around 134 cm^{-1}, which is assigned to the symmetrical stretching of InO_6 octahedra, gradually shifts to 128 cm^{-1} (Figure 3c, inset). As we hypothesized, the concentration of NaOL in the reaction flask, where the temperature is sufficient to dissociate it, appears to govern the [V_O] in the resulting nanocrystals. Given that the previously reported postsynthetic treatment with hydrogen to make black In_2O_3 led to a shift of the Raman peak from 132 to 130 cm^{-1}, the tunability of [V_O] in our case seems to be wider. To estimate [V_O], the occupation factor of the oxygen site was analyzed by the Rietveld refinement of XRD patterns (Figures 3d and S9 and Table S2). Similar to the results of Raman analysis, the [V_O] without the addition of NaOL and when all of NaOL was in precursor solution were almost identical at less than 1% of the oxygen sites. The vacancy population increased up to 9.3% as NaOL added in oleyl alcohol increased to 13.0 mmol. This estimate was close to that from EDS data (8.7%) for the same synthetic conditions (Figure S1). All of these observations imply that the initial [NaOL] in oleyl alcohol synthetic medium is the decisive factor that affects the [V_O] in the lattice.

Demonstration of Generality. Finally, we generalized this strategy to generate intrinsic defects in different systems. First, the variation of the spectator metal salt was tested using KOL instead of NaOL in the synthesis of In_2O_3 nanocrystals (Figure 4a). Based on our mechanistic understanding, we hypothesized that KOL could be more effective in introducing V_O because it can dissociate more easily compared to NaOL (Figure S10 and Table S3).[43,48] Even when we changed the spectator salt, though, we observed almost identical results. When all of 19.5 mmol KOL is included in the $In(RCOO)_3$ precursor solution, the color of the nanocrystal powder was light gray, while the addition of 13.0 mmol of KOL in oleyl alcohol and 6.5 mmol of KOL in the $In(RCOO)_3$ precursor resulted in black In_2O_3 nanocrystal powder. XRD data shows that they are the same bixbyite structure of In_2O_3, and no incorporation of K^+ into the lattice was found by EDS (Figures S11 and S12). Due to the presence of K^+, however, the shape of In_2O_3 nanocrystals changed to cubic, as reported in our previous study.[30] This result shows that the nanocrystal shape can be varied while independently tuning [V_O] using spectator metal salts. Raman spectral changes were also almost the same as when NaOL was added, but the shift of the peak at 130 cm^{-1} was more significant with KOL addition, which is indicative of more distortion of the lattice by V_O (Figure 4b). Next, we tested the effect of NaOL addition on γ-Fe_2O_3 nanocrystal synthesis considering the importance in various applications and the feasibility of synthesis using the same continuous injection method.[27,32,49,50] The synthesized γ-Fe_2O_3 nanocrystals made with 7.0 mmol addition of iron carboxylate precursor but no NaOL added were 22 nm with an octahedral shape (Figure 4c). The powder was dark brown, and representative Raman peaks at 346, 493, and 700 cm^{-1} were observed. Including the XRD pattern, these observations are consistent with previously reported features of γ-Fe_2O_3 (Figure 4d).[27,49] In contrast, the introduction of NaOL in oleyl alcohol resulted in a darker color close to pitch-black. In Raman spectra, not only were the relative peak intensities at 346 cm^{-1} and around 493 cm^{-1} reduced but also the location of the maximum peak intensity in the main broad peak shifted from 700 to 668 cm^{-1}. These Raman peaks and color are close to well-known characteristics of Fe_3O_4, which is indistinguishable from γ-Fe_2O_3 by XRD (Figure S11).[27,49] However, given that the Raman peak near 660 cm^{-1} is expected to be sharp in pure Fe_3O_4, the data suggest that the addition of NaOL in oleyl alcohol resulted in the partial reduction of γ-Fe_2O_3 forming a mixed phase with Fe_3O_4.[49] In fact, the ratio of iron to oxygen increased by 15% when NaOL was added in oleyl alcohol, with no incorporation of Na evident by EDS analysis (Figure S12). This reduction of γ-Fe_2O_3 nanocrystals is consistent with the formation of Fe_3O_4 by the reduction of γ-Fe_2O_3 reported previously.[27,51,52] We observed more vigorous reduction by the addition of NaOL in oleyl alcohol during CdO synthesis following a similar procedure. The CdO obtained without NaOL is octahedral in shape with crystallite sizes around 500 nm and a reddish brown color (Figure 4e). The introduction of 0.8 mmol of NaOL in the oleyl alcohol followed by the injection of the same cadmium precursor solution resulted in both deformation of particle shape and color change to light yellow-green. Even though it was a small amount compared to the amount of NaOL added in both In_2O_3 and γ-Fe_2O_3 studies, we found that the addition of NaOL generates a considerable amount of cadmium metal as a byproduct based on the XRD pattern (Figure S11). The increased relative amount of cadmium compared to that of oxygen from EDS also supports the formation of cadmium metal while no signal of Na was detected (Figure S12). This observation is consistent with previous observations that cadmium metal crystals are formed as a byproduct during CdO nanocrystal synthesis.[24] Considering that V_O can change the oxidation state of the cation in a metal oxide, the increased amount of cadmium metal can be driven by a high [V_O] generated due to the addition of NaOL.[27] Indeed, cadmium metal was the sole product detected when we increased the amount of NaOL in oleyl alcohol to 1.6 mmol (Figure S13). The formation of cadmium metal crystals increased extinction broadly in the IR region, but apparently the localized surface plasmon resonance peak from the remaining CdO was also shifted from 1650 to 2300 cm^{-1} (Figure 4f). This shift, and the change to a pale color, can be explained by an increase of free-electron concentration in the remaining CdO due to an increase in [V_O].[24]

■ CONCLUSIONS

We found that intrinsic defects can be deliberately generated by the addition of spectator salt during the synthesis of metal oxide nanocrystals. Due to the enhanced dissociation of carboxylates from metal cations in the precursor complex, the precursor becomes oxygen-deficient. This deficiency persists in the crystal lattice where V_O can be formed in different metal oxide materials, with independent tunability of their concentration and the morphology of the nanocrystals. Although the equilibrium [V_O] in metal oxides can be controlled by adjusting the partial pressure of oxygen, thus fixing the oxygen chemical potential,[40] the realization of homogeneously incorporated intrinsic defects is limited by slow diffusion kinetics in the solid state. Instead, we fix the chemical potential for $RCOO^-$ in the reaction solution, where a dynamic equilibrium readily establishes oxygen deficiency in the precursor complex, which is retained as the oxide crystal lattice forms. Since a variety of metal $RCOO^-$ complexes and ionic compounds have been used as precursors for nanocrystal synthesis, we expect that this principle can apply to a wide range of metal oxides and potentially other ionic semiconductor materials by choosing the right additive spectator metal salts. Even for the incorporation of extrinsic impurity defects, the tunable influence of ionic strength on precursor dissociation may prove a useful tool for controlling reactivity.[45] This strategy for intrinsic defect formation provides a new synthetic route for understanding and optimizing the catalytic, optical, and transport properties and tuning the ferroelectric and magnetic properties of metal oxides and potentially of recently emerging functional materials including halide perovskites, metal-organic frameworks, and topological insulators, where defects play an important role.[4,17]

■ EXPERIMENTAL SECTION

Materials. Indium(III) acetate, (In(ac)$_3$, 99.99%), iron(II) acetate (Fe(ac)$_2$, 99.99%), cadmium acetylacetonate (Cd(acac)$_2$, 99.9%), oleic acid (OA, 90%, technical grade), 1-octadecene (ODE, 90%, technical grade), oleyl alcohol (85%, technical grade), and oleylamine (Olam, 70%, technical grade) were purchased from Sigma-Aldrich and used as received. Sodium oleate (NaOL, >97%) and potassium oleate (KOL, >98%) were purchased from TCI America and used without further purification.

Nanocrystal Synthesis. *Preparation of In(RCOO)$_3$ Precursor Solution for In$_2$O$_3$ Nanocrystal Synthesis.* To synthesize In$_2$O$_3$ nanocrystals, 16 mL of OA (50.7 mmol) and 8 mL of ODE (25.0 mmol) were mixed in a 50 mL three-neck flask and heated to 160 °C with stirring. Then, 2.34 g of In(ac)$_3$ (8.0 mmol) was introduced. The final total volume of the prepared precursor solution was 24 mL. The flask was purged with a flowing nitrogen gas and heated for 1 h, yielding a transparent yellow solution.

Preparation of Reactor and Injection for In$_2$O$_3$ Nanocrystal Synthesis. Thirteen milliliters of oleyl alcohol (41.2 mmol) was introduced in a 100 mL three-neck flask and heated to 140 °C under vacuum for 1 h. Then, this flask was heated to 290 °C under a flowing nitrogen. Once the In(RCOO)$_3$ precursor solution was prepared, the solution was transferred to a 50 mL glass syringe and the syringe was installed in the syringe pump. After connecting the installed syringe to the reactor with a 16-gauge steel syringe needle, the injection of precursor solution was started with an injection rate of 0.2 mL/min and the injection volume was 21 mL. The final color of the solution is greenish-yellow. The resulting size of the nanocrystals was 23 nm. To obtain the 29 nm sized In$_2$O$_3$ nanocrystals, 24 mL of the In(RCOO)$_3$ precursor solution that contains 8.0 mmol of In(ac)$_3$, 11 mL of OA, and 13 mL of ODE was injected in the same manner.

Preparation of In(RCOO)$_3$ Precursor Solution for Black In$_2$O$_3$ Nanocrystal Synthesis. For black In$_2$O$_3$ nanocrystal synthesis, 1.98 g (6.5 mmol) of NaOL and 14 mL of OA (44.4 mmol) were mixed in a 50 mL three-neck flask and heated to 120 °C with stirring. After forming a homogeneous solution, 8 mL of ODE (25.0 mmol) was added and the flask was heated to 160 °C. Finally, 2.34 g of In(ac)$_3$ (8.0 mmol) was introduced and the final volume of precursor solution was 24 mL. The flask was purged with a nitrogen gas and heated for 1 h to get a transparent slightly yellow solution.

Preparation of Reactor and Injection for Black In$_2$O$_3$ Nanocrystal Synthesis. Thirteen milliliters of oleyl alcohol (41.2 mmol) and 3.96 g of NaOL (13.0 mmol) were introduced in a 100 mL three-neck flask and heated to 140 °C under vacuum for 1 h. Then, this flask was heated to 290 °C under a flowing nitrogen. Once the In(RCOO)$_3$ precursor solution was prepared, the solution was transferred to a 50 mL glass syringe and the syringe was installed in the syringe pump. After connecting the installed syringe to the reactor with a 16-gauge steel syringe needle, the injection of precursor solution was started with an injection rate of 0.2 mL/min and the injection volume was 21 mL. The solution color is black throughout the injection of In(RCOO)$_3$ precursor solution.

Preparation of Precursor Solution for Maghemite (γ-Fe$_2$O$_3$) Nanocrystal and Reduced Maghemite (γ-Fe$_2$O$_3$/Fe$_3$O$_4$) Nanocrystal Synthesis. Sixteen milliliters of OA (50.7 mmol) and 8 mL of ODE (25.0 mmol) were mixed in a 50 mL three-neck flask and heated to 160 °C with stirring. Then, 1.39 g of Fe(ac)$_2$ (8.0 mmol) was introduced. The flask was purged with a flowing nitrogen gas and heated for 1 h.

Preparation of Reactor and Injection for Maghemite (γ-Fe$_2$O$_3$) Nanocrystal Synthesis. Thirteen milliliters of oleyl alcohol (41.2 mmol) was introduced in a 100 mL three-neck flask and heated to 140 °C under vacuum for 1 h. Then, this flask was heated to 290 °C under a flowing nitrogen. When the precursor solution was prepared, the solution was transferred to a 50 mL glass syringe and the syringe was installed in the syringe pump. After connecting the installed syringe to the reactor with a 16-gauge steel syringe needle, the injection of precursor solution was started with an injection rate of 0.2 mL/min and the injection volume was 21 mL.

Preparation of Reactor and Injection for Reduced Maghemite (γ-Fe$_2$O$_3$/Fe$_3$O$_4$) Nanocrystal Synthesis. Thirteen milliliters of oleyl alcohol (41.2 mmol) and 3.96 g of NaOL (13.0 mmol) were introduced in a 100 mL three-neck flask and heated to 140 °C under vacuum for 1 h. Then, this flask was heated to 290 °C under a flowing nitrogen. Once the precursor solution was prepared, the syringe was installed in the syringe pump. After connecting the installed syringe to the reactor with a 16-gauge steel syringe needle, the injection of precursor solution was started with an injection rate of 0.2 mL/min and the injection volume was 19 mL.

Preparation of Precursor Solution for Cadmium Oxide (CdO) and Reduced CdO (Cd/CdO) Synthesis. As for some other metal oxides, the formation of CdO is inhibited when only OA was added to the precursor solution.[53,54] Therefore, we substituted 25% of OA with oleylamine (Olam) to promote CdO crystal formation. Six milliliters of OA (19.0 mmol), 2.1 mL of Olam (6.4 mmol), and 4 mL of ODE (12.5 mmol) were mixed in a 25 mL three-neck flask and heated to 150 °C with stirring. Note that CdO synthesis is inhibited in the absence of Olam. Then, 1.24 g of Cd(acac)$_2$ (4.0 mmol) was introduced. The flask was purged with a flowing nitrogen gas and heated for 2 h, yielding a transparent pale yellow-colored solution.

Preparation of Reactor and Injection for CdO Synthesis. Thirteen milliliters of oleyl alcohol (41.2 mmol) was introduced in a 100 mL three-neck flask and heated to 140 °C under vacuum for 1 h. Then, this flask was heated to 260 °C under a flowing nitrogen. When the precursor solution was prepared, the solution was transferred to a 50 mL glass syringe and the syringe was installed in the syringe pump. After connecting the installed syringe to the reactor with a 16-gauge steel syringe needle, the injection of precursor solution was started with an injection rate of 0.2 mL/min and the injection volume was 10 mL.

Preparation of Reactor and Injection for Cd/CdO Crystal Nanocrystal Synthesis. Thirteen milliliters of oleyl alcohol (41.2 mmol) and 0.24 g of NaOL (0.8 mmol) were introduced in a 100 mL three-neck flask and heated to 140 °C under vacuum for 1 h. Then, this flask was heated to 260 °C under a flowing nitrogen. Once the precursor solution was prepared, the syringe was installed in the syringe pump. After connecting the installed syringe to the reactor with a 16-gauge steel syringe needle, the injection of precursor solution was started with an injection rate of 0.2 mL/min and the injection volume was 10 mL.

Purification Procedure. After injection of each precursor solution, the temperature was maintained for 20 min before cooling to room temperature. After cooling down, 3 mL of hexane and 20 mL of reagent alcohol, which is primarily ethanol, were introduced to flocculate the solid contents. Then, the mixture was centrifuged at 5000 rpm for 5 min. After dispersing nanocrystals in 20 mL of hexane, 20 mL of methanol was introduced to remove the residual NaOL. After gently shaking, this solution was centrifuged at 5000 rpm. Even though methanol does not mix with hexane, the phase-separated mixture was effective as a washing solvent since the produced nanocrystals can anyway be flocculated under centrifugation at 5000 rpm, which we attribute to the low surface density of ligands and their large size. This step was repeated more than three times. Next, nanocrystals were dispersed in 10 mL of hexane and precipitated with the addition of 2 mL of ethanol. After gently agitating, this mixture was centrifuged again at 4000 rpm. After repeating one more cycle of washing steps with hexane and ethanol, the nanocrystals were finally dispersed in hexane.

■ ASSOCIATED CONTENT

Supporting Information

The Supporting Information is available free of charge at https://pubs.acs.org/doi/10.1021/jacs.2c08716.

> Characterization methods, classical MD simulation, EDS, XPS, TGA, XRD, and SEM data (PDF)

■ AUTHOR INFORMATION

Corresponding Author

Delia J. Milliron − *McKetta Department of Chemical Engineering, University of Texas at Austin, Austin, Texas 78712, United States; Department of Chemistry, University of Texas at Austin, Austin, Texas 78712, United States;* orcid.org/0000-0002-8737-451X; Email: milliron@che.utexas.edu

Authors

Kihoon Kim − *McKetta Department of Chemical Engineering, University of Texas at Austin, Austin, Texas 78712, United States;* orcid.org/0000-0003-1034-9233

Jiwon Yu − *McKetta Department of Chemical Engineering, University of Texas at Austin, Austin, Texas 78712, United States;* orcid.org/0000-0002-9861-0143

Jungchul Noh − *McKetta Department of Chemical Engineering, University of Texas at Austin, Austin, Texas 78712, United States*

Lauren C. Reimnitz − *McKetta Department of Chemical Engineering, University of Texas at Austin, Austin, Texas 78712, United States*

Matthew Chang − *Department of Chemistry, University of Washington, Seattle, Washington 98195-1700, United States;* orcid.org/0000-0002-1409-3194

Daniel R. Gamelin − *Department of Chemistry, University of Washington, Seattle, Washington 98195-1700, United States;* orcid.org/0000-0003-2888-9916

Brian A. Korgel − *McKetta Department of Chemical Engineering, University of Texas at Austin, Austin, Texas 78712, United States; Texas Materials Institute, University of Texas at Austin, Austin, Texas 78712, United States;* orcid.org/0000-0001-6242-7526

Gyeong S. Hwang − *McKetta Department of Chemical Engineering, University of Texas at Austin, Austin, Texas 78712, United States;* orcid.org/0000-0002-5538-9426

Complete contact information is available at: https://pubs.acs.org/10.1021/jacs.2c08716

Notes

The authors declare no competing financial interest.

■ ACKNOWLEDGMENTS

This research was supported by NSF (CHE-1905263 and CHE-1904436) and the Robert A. Welch Foundation (F-1848, F-1464, and F-1535). The authors acknowledge the Texas Advanced Computing Center (TACC) at the University of Texas at Austin for providing HPC resources that have contributed to the research results reported within this paper. The authors thank Dr. P. Banerjee for preliminary contributions to Rietveld analysis and Dr. N. Miller for contribution to ICP-MS analysis.

■ REFERENCES

(1) Agrawal, A.; Cho, S. H.; Zandi, O.; Ghosh, S.; Johns, R. W.; Milliron, D. J. Localized surface plasmon resonance in semiconductor nanocrystals. *Chem. Rev.* **2018**, *118*, 3121−3207.

(2) Beaulac, R.; Archer, P. I.; Ochsenbein, S. T.; Gamelin, D. R. Mn^{2+}-doped CdSe quantum dots: New inorganic materials for spin-electronics and spin-photonics. *Adv. Funct. Mater.* **2008**, *18*, 3873−3891.

(3) Beaulac, R.; Archer, P. I.; van Rijssel, J.; Meijerink, A.; Gamelin, D. R. Exciton storage by Mn^{2+} in colloidal Mn^{2+}-doped CdSe quantum dots. *Nano Lett.* **2008**, *8*, 2949−2953.

(4) Parobek, D.; Roman, B. J.; Dong, Y.; Jin, H.; Lee, E.; Sheldon, M.; Son, D. H. Exciton-to-dopant energy transfer in Mn-Doped cesium lead halide perovskite nanocrystals. *Nano Lett.* **2016**, *16*, 7376−7380.

(5) Kalinin, S. V.; Spaldin, N. A. Functional ion defects in transition metal oxides. *Science* **2013**, *341*, 858−859.

(6) Kan, D.; Terashima, T.; Kanda, R.; Masuno, A.; Tanaka, K.; Chu, S.; Kan, H.; Ishizumi, A.; Kanemitsu, Y.; Shimakawa, Y.; Takano, M. Blue-light emission at room temperature from Ar^+-irradiated $SrTiO_3$. *Nat. Mater.* **2005**, *4*, 816−819.

(7) Chen, X.; Liu, L.; Yu, P. Y.; Mao, S. S. Increasing solar absorption for photocatalysis with black hydrogenated titanium dioxide nanocrystals. *Science* **2011**, *331*, 746−750.

(8) Wang, L.; Dong, Y.; Yan, T.; Hu, Z.; Jelle, A. A.; Meira, D. M.; Duchesne, P. N.; Loh, J. Y. Y.; Qiu, C.; Storey, E. E.; et al. Black indium oxide a photothermal CO_2 hydrogenation catalyst. *Nat. Commun.* **2020**, *11*, No. 2432.

(9) Zhang, Z.; Mao, C.; Meira, D. M.; Duchesne, P. N.; Tountas, A. A.; Li, Z.; Qiu, C.; Tang, S.; Song, R.; Ding, X.; et al. New black indium oxide−andem photothermal CO_2-H_2 methanol selective catalyst. *Nat. Commun.* **2022**, *13*, No. 1512.

(10) Wang, X.; Guo, L. SERS activity of semiconductors: crystalline and amorphous nanomaterials. *Angew. Chem., Int. Ed.* **2020**, *59*, 4231−4239.

(11) Xiao, Z.; Huang, Y.-C.; Dong, C.-L.; Xie, C.; Liu, Z.; Du, S.; Chen, W.; Yan, D.; Tao, L.; Shu, Z.; et al. Operando identification of the dynamic behavior of oxygen vacancy-rich Co_3O_4 for oxygen evolution reaction. *J. Am. Chem. Soc.* **2020**, *142*, 12087−12095.

(12) Li, Z.; Zhou, C.; Hua, J.; Hong, X.; Sun, C.; Li, H.-W.; Xu, X.; Mai, L. Engineering oxygen vacancies in a polysulfide-blocking layer with enhanced catalytic ability. *Adv. Mater.* **2020**, *32*, No. 1907444.

(13) Dang, S.; Qin, B.; Yang, Y.; Wang, H.; Cai, J.; Han, Y.; Li, S.; Gao, P.; Sun, Y. Rationally designed indium oxide catalysts for CO_2 hydrogenation to methanol with high activity and selectivity. *Sci. Adv.* **2020**, *6*, No. eaaz2060.

(14) Lu, G.; Linsebigler, A.; Yates, J. T., Jr Photooxidation of CH_3Cl on TiO_2 (110): A mechanism not involving H_2O. *J. Phys. Chem. A* **1995**, *99*, 7626−7631.

(15) Greiner, M. T.; Chai, L.; Helander, M. G.; Tang, W.-M.; Lu, Z.-H. Transition metal oxide work functions: The influence of cation oxidation state and oxygen vacancies. *Adv. Funct. Mater.* **2012**, *22*, 4557−4568.

(16) Wang, Z.; Wang, L. Role of oxygen vacancy in metal oxide based photoelectrochemical water splitting. *EcoMat* **2021**, *3*, No. e12075.

(17) Walsh, A.; Zunger, A. Instilling defect tolerance in new compounds. *Nat. Mater.* **2017**, *16*, 964−967.

(18) Galli, G. Doping the undopable. *Nature* **2005**, *436*, 32−33.

(19) Erwin, S. C.; Zu, L.; Haftel, M. I.; Efros, A. L.; Kennedy, T. A.; Norris, D. J. Doping semiconductor nanocrystals. *Nature* **2005**, *436*, 91−94.

(20) Jansons, A. W.; Hutchison, J. E. Continuous growth of metal oxide nanocrystals: Enhanced control of nanocrystal size and radial dopant distribution. *ACS Nano* **2016**, *10*, 6942−6951.

(21) Gibbs, S. L.; Dean, C.; Saad, J.; Tandon, B.; Staller, C. M.; Agrawal, A.; Milliron, D. J. Dual-mode infrared absorption by segregating dopants within plasmonic semiconductor nanocrystals. *Nano Lett.* **2020**, *20*, 7498−7505.

(22) Chen, H.-Y.; Maiti, S.; Son, D. H. Doping location-dependent energy transfer dynamics in Mn-doped CdS/ZnS nanocrystals. *ACS Nano* **2012**, *6*, 583−591.

(23) Gordon, T. R.; Cargnello, M.; Paik, T.; Mangolini, F.; Weber, R. T.; Fornasiero, P.; Murray, C. B. Nonaqueous synthesis of TiO_2 nanocrystals using TiF_4 to engineer morphology, oxygen vacancy concentration, and photocatalytic activity. *J. Am. Chem. Soc.* **2012**, *134*, 6751−6761.

(24) Liu, Z.; Zhong, Y.; Shafei, I.; Jeong, S.; Wang, L.; Nguyen, H. T.; Sun, C.-J.; Li, T.; Chen, J.; Chen, L.; et al. Broadband tunable mid-infrared plasmon resonances in cadmium oxide nanocrystals induced by size-dependent nonstoichiometry. *Nano Lett.* **2020**, *20*, 2821−2828.

(25) Tuller, H. L.; Bishop, S. R. Point defects in oxides: Tailoring materials through defect engineering. *Annu. Rev. Mater. Res.* **2011**, *41*, 369−398.

(26) De Wit, J. Electrical properties of In_2O_3. *J. Solid State Chem.* **1973**, *8*, 142−149.

(27) Jung, H.; Schimpf, A. M. Photochemical reduction of nanocrystalline maghemite to magnetite. *Nanoscale* **2021**, *13*, 17465−17472.

(28) Morgan, B. J.; Watson, G. W. A density functional theory+ U study of oxygen vacancy formation at the (110), (100), (101), and (001) surfaces of rutile TiO_2. *J. Phys. Chem. C* **2009**, *113*, 7322−7328.

(29) Perevalov, T.; Aliev, V. S.; Gritsenko, V.; Saraev, A.; Kaichev, V. Electronic structure of oxygen vacancies in hafnium oxide. *Microelectron. Eng.* **2013**, *109*, 21−23.

(30) Kim, K.; Reimnitz, L. C.; Cho, S. H.; Noh, J.; Dong, Z.; Gibbs, S. L.; Korgel, B. A.; Milliron, D. J. Effect of Nonincorporative Cations on the Size and Shape of Indium Oxide Nanocrystals. *Chem. Mater.* **2020**, *32*, 9347−9354.

(31) Jansons, A. W.; Koskela, K. M.; Crockett, B. M.; Hutchison, J. E. Transition metal-doped metal oxide nanocrystals: Efficient substitutional doping through a continuous growth process. *Chem. Mater.* **2017**, *29*, 8167−8176.

(32) Ito, D.; Yokoyama, S.; Zaikova, T.; Masuko, K.; Hutchison, J. E. Synthesis of ligand-stabilized metal oxide nanocrystals and epitaxial core/shell nanocrystals via a lower-temperature esterification process. *ACS Nano* **2014**, *8*, 64−75.

(33) Gan, J.; Lu, X.; Wu, J.; Xie, S.; Zhai, T.; Yu, M.; Zhang, Z.; Mao, Y.; Wang, S. C. I.; Shen, Y.; Tong, Y. Oxygen vacancies promoting photoelectrochemical performance of In_2O_3 nanocubes. *Sci. Rep.* **2013**, *3*, No. 1021.

(34) Arooj, S.; Xu, T.; Hou, X.; Wang, Y.; Tong, J.; Chu, R.; Liu, B. Green emission of indium oxide via hydrogen treatment. *RSC Adv.* **2018**, *8*, 11828−11833.

(35) Zheng, M. J.; Zhang, L.-D.; Li, G.-H.; Zhang, X. Y.; Wang, X. Ordered indium-oxide nanowire arrays and their photoluminescence properties. *Appl. Phys. Lett.* **2001**, *79*, 839−841.

(36) Naldoni, A.; Allieta, M.; Santangelo, S.; Marelli, M.; Fabbri, F.; Cappelli, S.; Bianchi, C. L.; Psaro, R.; Dal Santo, V. Effect of nature and location of defects on bandgap narrowing in black TiO_2 nanoparticles. *J. Am. Chem. Soc.* **2012**, *134*, 7600−7603.

(37) Kitajima, M. Defects in crystals studied by Raman scattering. *Crit. Rev. Solid State Mater. Sci.* **1997**, *22*, 275−349.

(38) Arora, A. K.; Rajalakshmi, M.; Ravindran, T.; Sivasubramanian, V. Raman spectroscopy of optical phonon confinement in nanostructured materials. *J. Raman Spectrosc.* **2007**, *38*, 604−617.

(39) Lee, Y.; He, G.; Akey, A. J.; Si, R.; Flytzani-Stephanopoulos, M.; Herman, I. P. Raman analysis of mode softening in nanoparticle $CeO_{2-\delta}$ and Au-$CeO_{2-\delta}$ during CO oxidation. *J. Am. Chem. Soc.* **2011**, *133*, 12952−12955.

(40) Chatratin, I.; Sabino, F. P.; Reunchan, P.; Limpijumnong, S.; Varley, J. B.; Van de Walle, C. G.; Janotti, A. Role of point defects in the electrical and optical properties of In_2O_3. *Phys. Rev. Mater.* **2019**, *3*, No. 074604.

(41) Ágoston, P.; Erhart, P.; Klein, A.; Albe, K. Geometry, electronic structure and thermodynamic stability of intrinsic point defects in indium oxide. *J. Phys.: Condens. Matter* **2009**, *21*, No. 455801.

(42) Narayanaswamy, A.; Xu, H.; Pradhan, N.; Kim, M.; Peng, X. Formation of nearly monodisperse In_2O_3 nanodots and oriented-attached nanoflowers: hydrolysis and alcoholysis vs pyrolysis. *J. Am. Chem. Soc.* **2006**, *128*, 10310−10319.

(43) Kovalenko, M. V.; Bodnarchuk, M. I.; Lechner, R. T.; Hesser, G.; Schäffler, F.; Heiss, W. Fatty acid salts as stabilizers in size-and shape-controlled nanocrystal synthesis: The case of inverse spinel iron oxide. *J. Am. Chem. Soc.* **2007**, *129*, 6352−6353.

(44) Shavel, A.; Liz-Marzán, L. M. Shape control of iron oxide nanoparticles. *Phys. Chem. Chem. Phys.* **2009**, *11*, 3762−3766.

(45) Buonsanti, R.; Milliron, D. J. Chemistry of doped colloidal nanocrystals. *Chem. Mater.* **2013**, *25*, 1305−1317.

(46) Gibson, N. J.; Bredar, A. R. C.; Chakraborty, N.; Farnum, B. H. Group 13 Lewis acid catalyzed synthesis of metal oxide nanocrystals via hydroxide transmetallation. *Nanoscale* **2021**, *13*, 11505−11517.

(47) Sänze, S.; Gurlo, A.; Hess, C. Monitoring gas sensors at work: Operando Raman-FTIR study of ethanol detection by indium oxide. *Angew. Chem., Int. Ed.* **2013**, *52*, 3607−3610.

(48) Marcus, Y.; Hefter, G. Ion pairing. *Chem. Rev.* **2006**, *106*, 4585−4621.

(49) Testa-Anta, M.; Ramos-Docampo, M. A.; Comesaña-Hermo, M.; Rivas-Murias, B.; Salgueiriño, V. Raman spectroscopy to unravel the magnetic properties of iron oxide nanocrystals for bio-related applications. *Nanoscale Adv.* **2019**, *1*, 2086−2103.

(50) Qiu, K.; Chai, G.; Jiang, C.; Ling, M.; Tang, J.; Guo, Z. Highly efficient oxygen reduction catalysts by rational synthesis of nanoconfined maghemite in a nitrogen-doped graphene framework. *ACS Catal.* **2016**, *6*, 3558−3568.

(51) Sun, Y.-K.; Ma, M.; Zhang, Y.; Gu, N. Synthesis of nanometer-size maghemite particles from magnetite. *Colloids Surf., A* **2004**, *245*, 15−19.

(52) Yamazaki, T.; Solheid, P. Maghemite-to-magnetite reduction across the Fe-redox boundary in a sediment core from the Ontong-Java Plateau: Influence on relative palaeointensity estimation and environmental magnetic application. *Geophys. J. Int.* **2011**, *185*, 1243−1254.

(53) Wainer, P.; Kendall, O.; Lamb, A.; Barrow, S. J.; Tricoli, A.; Gómez, D. E.; van Embden, J.; Della Gaspera, E. Continuous growth synthesis of zinc oxide nanocrystals with tunable size and doping. *Chem. Mater.* **2019**, *31*, 9604−9613.

(54) Hofmann, C.; Rusakova, I.; Ould-Ely, T.; Prieto-Centurión, D.; Hartman, K. B.; Kelly, A. T.; Lüttge, A.; Whitmire, K. H. Shape control of new Fe_xO-Fe_3O_4 and $Fe_{1-y}Mn_yO$-$Fe_{3-z}Mn_zO_4$ nanostructures. *Adv. Funct. Mater.* **2008**, *18*, 1661−1667.